LETTERS
https://doi.org/10.1038/s41587-019-0403-9

nature biotechnology

There are amendments to this paper

A computationally designed chimeric antigen receptor provides a small-molecule safety switch for T-cell therapy

Greta Giordano-Attianese[1,2,6], Pablo Gainza[3,4,6], Elise Gray-Gaillard[1,2,6], Elisabetta Cribioli[1,2], Sailan Shui[3,4], Seonghoon Kim[5], Mi-Jeong Kwak[5], Sabrina Vollers[3,4], Angel De Jesus Corria Osorio[1,2], Patrick Reichenbach[1,2], Jaume Bonet[3,4], Byung-Ha Oh[5], Melita Irving[1,2,7]*, George Coukos[1,2,7]* and Bruno E. Correia[3,4,7]*

Approaches to increase the activity of chimeric antigen receptor (CAR)-T cells against solid tumors may also increase the risk of toxicity and other side effects. To improve the safety of CAR-T-cell therapy, we computationally designed a chemically disruptable heterodimer (CDH) based on the binding of two human proteins. The CDH self-assembles, can be disrupted by a small-molecule drug and has a high-affinity protein interface with minimal amino acid deviation from wild-type human proteins. We incorporated the CDH into a synthetic heterodimeric CAR, called STOP-CAR, that has an antigen-recognition chain and a CD3ζ- and CD28-containing endodomain signaling chain. We tested STOP-CAR-T cells specific for two antigens in vitro and in vivo and found similar antitumor activity compared to second-generation (2G) CAR-T cells. Timed administration of the small-molecule drug dynamically inactivated the activity of STOP-CAR-T cells. Our work highlights the potential for structure-based design to add controllable elements to synthetic cellular therapies.

T cells engineered with CARs, hybrid molecules linking antigen binding to T-cell signaling endodomains, have mediated potent and durable responses against both chronic and acute B cell leukemias[1–4]. CAR-T cell therapy, however, is frequently associated with life-threatening side effects, including cytokine release syndrome (CRS) and neurotoxicity. The clinical development of CAR-T cells against solid tumors has proven challenging, but there is great optimism that next-generation CAR-T cells will bring benefit to a broader range of cancer patients[5]. Indeed, it is now well understood that physical and immunometabolic barriers upregulated in the solid tumor microenvironment as well as prolonged exposure to antigens can impair T-cell function and drive T-cell exhaustion[6]. Innovative engineering strategies, such as the expression of cytokines, chemokines, decoy molecules or stimulatory ligands, are being developed to overcome these obstacles and have shown favorable preclinical responses[6–8]. Safety, however, remains an important barrier to clinical entry because most solid tumor antigens targeted to date are also found in healthy tissues, sometimes leading to serious on-target off-tumor toxicity[9]. The ability to control CAR-T cell activity on command could greatly accelerate the clinical development of cellular immunotherapies.

The above considerations have driven the development of CAR-T cell control and safety systems[5], such as drug-inducible suicide switches[10,11], coinhibitory receptor (i)CARs that upon engagement with specific antigens suppress effector function[12] and split-signaling CAR-T cells that require co-engagement of two ligands for full T-cell activation[13]. SUPRA (split, universal and programmable) CARs[14] and a variety of universal CARs[15,16] have been developed that require administration of an adaptor protein to link nontumor antigen binding CAR-T cells to tumor cells. While these approaches offer the possibility to sequentially target different tumor antigens (for example, upon clonal escape), disadvantages to the use of adaptor proteins include the cost of recombinant protein production, potential immunogenicity upon repeated administration and insufficient tumor penetration and half-life. More recently, the feasibility of ON-switch CARs, requiring small-molecule-mediated heterodimerization to enable T-cell activation in the presence of antigen, has been demonstrated[17], but short half-life of the small molecule is an issue. Here, we present a computationally designed STOP-switch CAR-T cell control system, in which antigen binding and T-cell activation are encoded by two chains, the recognition (R) and the signaling (S) chains, respectively. These chains spontaneously dimerize into a functional heterodimer via a computationally designed protein pair inserted in the endodomains of the two CAR chains. The dimer can be specifically disrupted by administration of a small-molecule (Fig. 1a). Thus, STOP-CARs offer the possibility of transiently tuning down T-cell effector function, rather than completely eliminating the therapy, as in the case of a suicide switch.

With the aim of advancing STOP-CARs with potential for clinical translation, we sought to develop a CDH (a protein heterodimer that can be dissociated into two monomers by a small-molecule disruptor), comprising proteins of human origin with a minimal number of amino acid substitutions, to lessen the risk of transgene immune rejection in patients[18–20]. In addition, we wanted to use well-folded globular domains from proteins that should be modular and not interfere with synapse-proximal T-cell signaling. Finally, we initiated the CDH design based on the availability of clinically applicable disruptive small molecules that have a long half-life (>10 h) and are well tolerated in humans. Previously described CDH-like

[1]Ludwig Institute for Cancer Research, University of Lausanne (UNIL), Epalinges, Switzerland. [2]Department of Oncology, University Hospital of Lausanne (CHUV), Lausanne, Switzerland. [3]Institute of Bioengineering, École Polytechnique Fédérale de Lausanne (EPFL), Lausanne, Switzerland. [4]Swiss Institute of Bioinformatics (SIB), Lausanne, Switzerland. [5]Department of Biological Sciences, Institute for the Biocentury, Korea Advanced Institute of Science and Technology (KAIST), Daejeon, Korea. [6]These authors contributed equally: Greta Giordano-Attianese, Pablo Gainza, Elise Gray-Gaillard. [7]These authors jointly supervised this work: Melita Irving, George Coukos, Bruno E. Correia. *e-mail: melita.irving@unil.ch; george.coukos@unil.ch; bruno.correia@epfl.ch

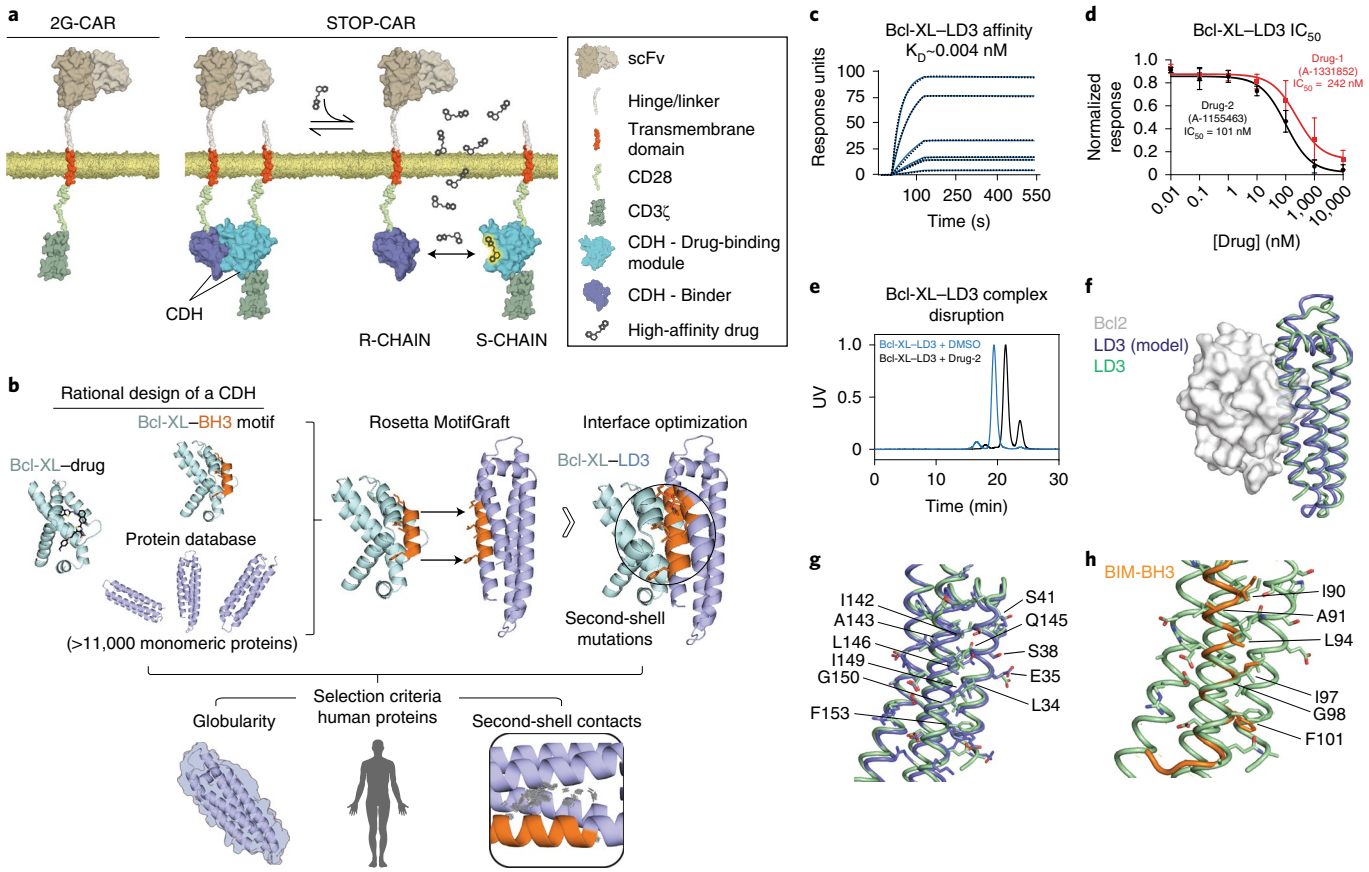

Fig. 1 | Structure-based computational design of a high-affinity CDH to control CAR-T-cell activity. a, Domain architectures of the classical 2G-CAR and the STOP-CAR. The CDH is spontaneously assembled by the drug-binding module (cyan) and the binder (dark blue), while it monomerizes in the presence of the drug disruptor. **b**, A 12-residue amino acid fragment from the BIM-BH3 domain interacting with Bcl-XL was matched against a database of >11,000 proteins using the MotifGraft program. Grafted scaffolds, selected for compatibility with Bcl-XL, were then designed, with their amino acid identities restricted to common substitutions according to the BLOSUM62 matrix. Designed scaffolds were filtered by three criteria: proteins with globularity, human origin (or with a close human homolog) and packing of the BH3 motif within the scaffold. **c**, SPR measurements for LD3–Bcl-XL binding interaction; analyte concentrations ranged from 7.8 nM to 250 nM. Sensorgrams and fitted curves are shown in dotted black and solid blue lines, respectively. Biological replicates were performed ($n=2$) with similar results. **d**, Apparent IC_{50}s of the LD3–Bcl-XL complex for the two drugs determined by SPR. Two Bcl-XL inhibitors were selected as candidates for the CDH disruption. Values are mean ± s.e.m. ($n=3$ biological replicates) **e**, SEC-MALS analysis. Bcl-XL–LD3 mixed with DMSO to form a heterodimer (blue trace), whereas Bcl-XL–LD3 mixed with Drug-2 did not result in a complex formation, with the two proteins eluting in the monomeric state (black trace). Biological replicates were performed ($n=2$) with similar results. **f**, The crystal structure of LD3 (pale green) in complex with the protein Bcl-2 (white) was in close agreement with the computational model of LD3 (dark blue) in complex with Bcl-XL (not shown); interface r.m.s.d. of 1.35 Å. **g**, Interface residues of LD3, including those transplanted from the BH3 motif, are labeled and shown as sticks in the model (dark blue) and the crystal structure (pale green). **h**, Crystal structure of the designed LD3 (pale green) versus the natural BIM-BH3 peptide (orange) with the hotspot residues shown as sticks.

systems have not met these criteria, either because the proteins were not of human origin, were modulated by endogenous molecules such as biotin[21] or had weak binding affinity[22].

We identified the interaction between human Bcl-XL (B cell lymphoma extra large; a transmembrane mitochondrial protein with anti-apoptotic activity) and the BH3 (Bcl-2 homology 3) domain[23] of BIM (Bcl-2-interacting mediator of cell death; a pro-apoptotic molecule) as a promising starting point for the CDH design, with the intent of incorporating Bcl-XL in the endodomain of the S-chain and the BIM domain in the R-chain. Several drugs with clinical potential are available that can inhibit their interaction[24]. The BIM protein is an intrinsically unstructured, nonglobular protein in its unbound state. Using computational protein design, we aimed to replace BIM with a high-affinity globular protein, which can be modularly installed in synthetic constructs. Our computational strategy consisted of transplanting the BH3 binding motif from the intrinsically disordered BH3 segment of BIM[25] onto a human globular domain to bind Bcl-XL with high affinity. Notably, an important challenge is that the affinity of BH3 domains and Bcl-2 family proteins (Bcl-XL and Bcl-2) depends not only on helical residues that form the interface's hydrophobic core, but also on polar residues pointing away from it[26]. Indeed, previous attempts to design Bcl-2-family binding proteins by engrafting the BH3 domain onto pre-existing scaffolds have yielded weaker binders than the native, unstructured BH3 domain itself[26–28].

To develop the CDH we used the computational tool Rosetta MotifGraft[29] to redesign existing monomeric proteins to bind to Bcl-XL. Briefly, MotifGraft performs extensive structural searches in protein databases to identify scaffolds with backbone similarity to a binding motif, as well as structural compatibility to a given binding partner (Supplementary Fig. 1a,b). Subsequently, MotifGraft transplants critical binding residues and performs additional design at interface residues. The structure of Bcl-XL in complex with BIM-BH3 peptide (Protein Data Bank (PDB) ID: 3FDL; Fig. 1b) was used as input and the 12-amino acid helical segment from BIM-BH3 (Fig. 1b), IAXXLXXIGXXF, as the binding motif

(hotspot residues are underlined)[25]. Residues within 6 Å of Bcl-XL were conservatively designed, allowing only favorable substitutions according to the BLOSUM62 matrix. Designs that passed an initial steric filter were ranked by a predicted interaction energy (ΔΔG), filtered for globularity of the scaffold and packing of the binding motif against the scaffold (see Methods). Three lead designs (LDs) were generated: a rat protein with a close human homolog, syntaxin 6 (LD1), as well as two human proteins, human focal adhesion targeting domain of Pyk2 (LD2) and human apolipoprotein E4 (LD3) (Fig. 1b). The designs carried between 11 and 13 substitutions relative to the native proteins, which included six hotspot residues (Supplementary Fig. 1c).

The three computationally designed proteins were expressed recombinantly, biochemically characterized (Supplementary Fig. 2b,c) and their dissociation constant (K_d) for Bcl-XL assessed by surface plasmon resonance (SPR). LD1 and LD3 bound with K_d of 17 nM and 3.9 pM, respectively, while there was no detectable binding by LD2 (Fig. 1c and Supplementary Fig. 2a). In comparison, the previously reported K_d for the wild-type Bcl-XL–BIM-BH3 interaction was approximately 6 nM (ref. [30]). Two known small molecules, A1331852 and A1155463 (hereafter referred to as Drug-1 and Drug-2), have been reported to bind to Bcl-XL at less than 10 pM (ref. [24]) and were shown by SPR and size-exclusion chromatography coupled to a multi-angle light scatter (SEC-MALS) to dissociate Bcl-XL from LD3 (Fig. 1d,e), with an apparent half-maximum inhibitory concentration (IC_{50}) of 242 nM and 101 nM (Fig. 1d and Supplementary Fig. 2d), respectively. On the basis of its favorable properties as a CDH, LD3 was chosen for further study. While it was not possible to obtain crystals of the LD3–Bcl-XL complex suitable for diffraction, a 2.5-Å crystal structure of LD3–Bcl-2 (a close homolog of Bcl-XL) was solved (Fig. 1f and Supplementary Fig. 3). The structure validated the computational model, as the solved LD3–Bcl-2 complex showed a root mean square deviation (r.m.s.d.) of 1.3 Å for the C_α atoms of the predicted model, 1.35 Å for the side chains of the designed interface (Fig. 1g) and 1.2 Å r.m.s.d. over the helical residues of the binding motif derived from BIM-BH3 (Fig. 1h).

We next sought to incorporate the CDH into a STOP-CAR design, under the hypothesis that the R- and S-chains containing LD3 and Bcl-XL, respectively, would self-assemble into a fully functional heterodimer, but LD3 would be displaced from Bcl-XL in the presence of a Bcl-XL inhibitor, disrupting T-cell activity. Indeed, the separation of antigen recognition from signal-transducing elements on separate receptors is a common feature of both the innate and adaptive immune system, as it enables genes encoding the ligand-binding receptor to diversify while maintaining signaling features[31]. For all designs tested, the R-chain ectodomain (Fig. 2a) contained the J591 single-chain variable antibody fragment (scFv) targeting the prostate-specific membrane antigen (PSMA)[32–34], an antigen expressed in a large proportion of advanced prostate adenocarcinomas, on the vascular endothelium of many solid tumors, but also in normal organs such as the duodenum and salivary glands. The R-chain also contained a CD8α hinge/linker (H/L), a CD28 transmembrane domain (TMD) and an intracytoplasmic domain, including the co-stimulatory endodomain (ED) from CD28, followed by LD3. For the S-chain, however, we tested three ectodomain variations (Supplementary Fig. 4a,g), each linked to a CD8α H/L, a TMD and co-stimulatory ED derived from CD28, followed by Bcl-XL, and finally the ED of CD3ζ at its terminus (Fig. 2a).

In our first STOP-CAR prototype, the S-chain ectodomain comprised only a c-Myc-tag, revealing high and stable transfection in Jurkat 6xNFAT-mCherry reporter cells (≈100% expression on day 15) using a single lentiviral vector, encoding both chains (Supplementary Fig. 4a). The chains localized on the cell membrane (Supplementary Fig. 4b) and Jurkat cells transduced with both chains of the STOP-CAR heterodimer (but not with either chain alone) were specifically activated in the presence of $PSMA^+$ target cells (Supplementary Fig. 4c,d). Stability of Jurkat transfection, however, as well as transduction of primary human T cells was poor for the S-chain (<5%) with the first prototype (Supplementary Fig. 4e,f). Assuming that the ectodomain of S-chain was responsible for chain instability, we added a CH2-CH3 linker (Supplementary Fig. 4g). This construct, however, was expressed at lower levels on Jurkat cells and was nearly undetectable on transduced primary T cells (<3% expression; Supplementary Fig. 4h).

In our next attempt to improve S-chain expression, we incorporated the ectodomain of DAP10, a signaling subunit broadly expressed by immune cells[31] (Fig. 2a). Here, we detected high levels of co-expression (>75% for both chains on day 15) on the surface of Jurkat reporter cells (Fig. 2b), sufficiently stable expression of both chains over 30 d (Fig. 2c and Supplementary Fig. 5b) and reporter activation upon antigen engagement (Fig. 2d). This design enabled satisfactory transduction efficiencies also in primary human $CD8^+$ and $CD4^+$ T cells (Fig. 2e and Supplementary Fig. 5c,d). Transduction did not affect T-cell expansion (Fig. 2f) and both chains were stably expressed over 30 d (Fig. 2g). Although the inclusion of an endogenous T-cell ectodomain (DAP10) may enable T-cell activation through interaction with DAP10 ligands, this domain has been successfully used in CAR constructs[17]. Because DAP10 inclusion resulted in improved expression of the S-chain, we adopted this construct for further characterization.

We next tested the function of engineered primary human STOP-CAR-T cells. For these assays, we titrated down the 2G-CAR-T cells with untransduced (UTD) T cells, to match the frequency of T cells expressing the STOP-CAR (Supplementary Fig. 5d). We observed specific activation of the T cells engineered with STOP-CAR only

Fig. 2 | Computationally designed heterodimeric STOP-CARs are stably expressed on the surface of Jurkat and primary human T cells. a, Architecture of the STOP-CAR. Left: cartoon depicting the different components and the designed CDH formed by LD3 (dark blue) and Bcl-XL (cyan) in the monomeric disassembled form, forced by the drug disruptor. Right: schematic of the R- and S-chains encoded in a single lentiviral vector, each led by a CD8α leader sequence and separated by the T2A self-cleaving peptide. **b**, Flow cytometric evaluation of R- and S-chain expression on Jurkat cells detected by anti-human F(ab') Ab-APC (binds the scFv) and anti-c-Myc Ab-APC, respectively. UTD (blue) and CAR-positive (red) are shown. Two technical replicates were performed with similar results. Cell-surface colocalization of R- and S-chains, detected by anti-human F(ab') Ab-FITC and anti-c-Myc Ab-APC, respectively, using AMNIS imaging. Four representative Jurkat cells are shown, with the experiment performed once. Side scatter (SSC) in units in which $K = 1{,}000$. **c**, STOP-CAR stability on Jurkat cells by flow cytometric analysis. Values are reported as the mean of $n = 2$ technical replicates. **d**, Activation of the STOP-CAR-engineered Jurkat reporter cell line as measured by mCherry expression in the presence of a MS1-$PSMA^+$ target cell line. Values are reported as the mean of $n = 2$ technical replicates. The effector to target cell ratio was 1:1 and PMA and ionomycin-stimulated cells were set at 100%. **e**, Transduction efficiency of primary human T cells with vector carrying an anti-PSMA 2G-CAR or the full STOP-CAR. UTD (blue) and CAR-positive (red) are shown. Values are the mean ± s.e.m. of $n = 13$ human donors. **f**, Fold expansion of UTD-T cells and STOP-CAR-T cells is similar. Values are the mean ± s.e.m. of $n = 5$ human donors. **g**, Expression level of the STOP-CAR after 5, 15 and 30 d. Values are the mean ± s.e.m. of $n = 3$ human donors. **h**, A 48-h in vitro cytotoxicity assay of UTD-, STOP- or 2G-CAR-T cells (all tested 30 d after CAR transduction) against $PSMA^+$ PC3-PIP prostate cancer cells. Values are the mean ± s.e.m. of $n = 3$ human donors. One-way ANOVA was used for statistical analysis. Statistical significance: UTD versus 2G-CAR-T cells and UTD versus STOP-CAR-T cells; $^{****}P \leq 0.0001$.

in the presence of PSMA-transduced PC3 (PC3-PIP) cells, but not of PSMA-negative PC3 control prostate cancer cells ($n=4–5$ donors)[32] (Fig. 3a and Supplementary Fig. 6a–c) and observed similar cytokine and granzyme release by STOP- and 2G-CAR-T cells (Supplementary Fig. 6c,d). Furthermore, T cells transduced with anti-PSMA STOP-CAR 30 d earlier displayed important cytolytic activity in vitro against PC3-PIP(Fig. 2h).

Next, we tested whether STOP-CAR-T cells can be modulated by disruptor drugs. We identified 10 µM as the maximal dose of Drug-1 or Drug-2 that did not directly affect PC3-PIP cells (Supplementary Fig. 7a) and limited all in vitro experiments to this maximal dose. We also confirmed that neither drug was toxic to T cells at 10 µM (Supplementary Fig. 7b,c). We then conducted time-lapse killing assays, starting with bulk populations of transduced STOP-CAR-T

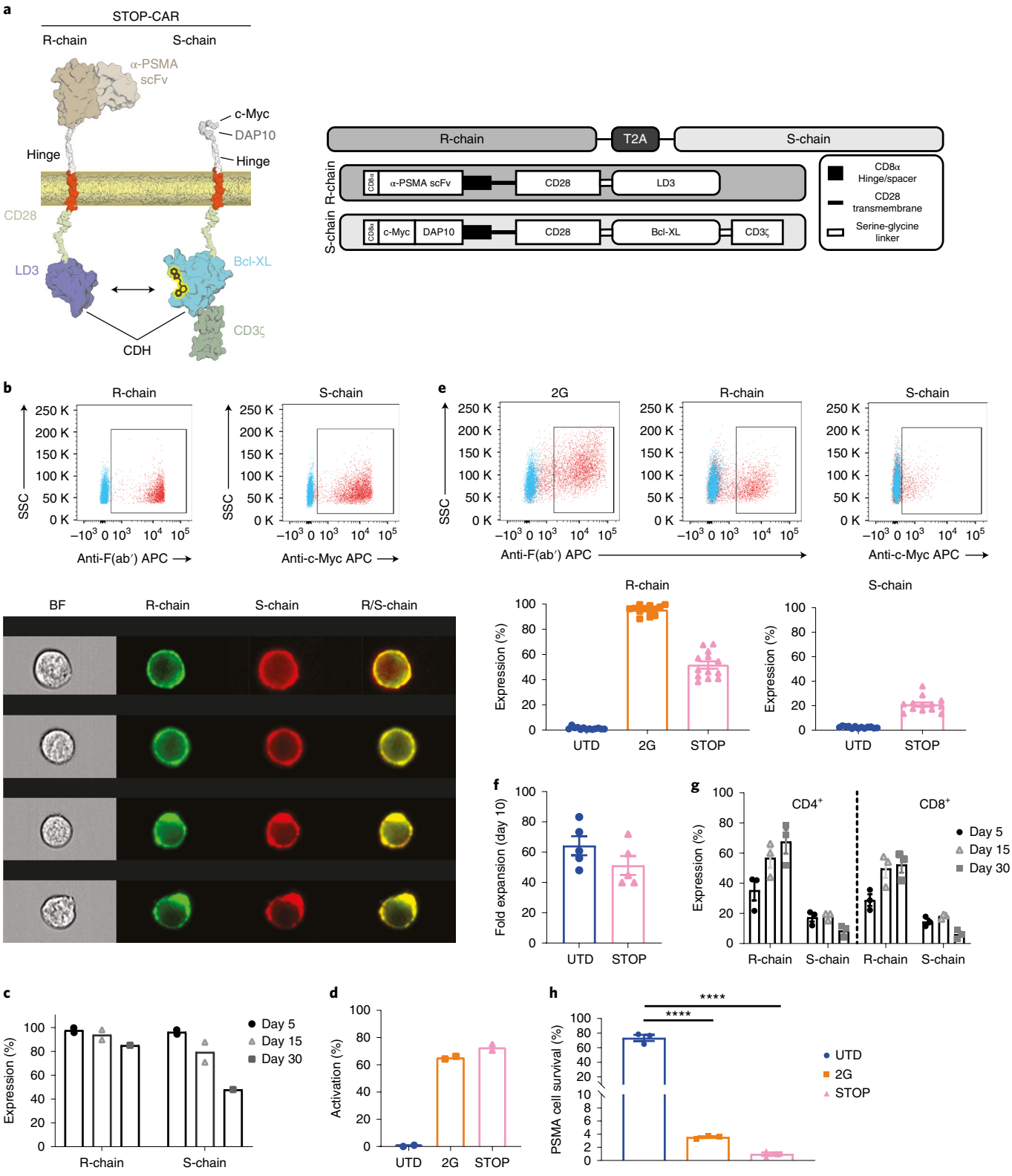

or 2G-T cells, used at similar frequencies, both exhibiting mostly effector and memory differentiation (Supplementary Fig. 5e). Addition of 10 μM Drug-2 specifically impaired the activation and cytotoxicity of STOP-CAR-T cells in vitro against PC3-PIP cells, but not of 2G-CAR-T cells (Fig. 3b). Drug-1 was not effective at 10 μM (Supplementary Fig. 8a), whereas lower concentrations of Drug-2 (5 μM) impaired the activity of STOP-CAR-T cells to a lesser extent than at 10 μM (Supplementary Fig. 8b).

We further assessed STOP-CAR-T and 2G-CAR-T activity against 22Rv1 cells, a prostate cancer cell line with natural expression of PSMA (Supplementary Fig. 9a). CAR-engineered Jurkat and primary human T cells were specifically activated by 22Rv1, as measured by the mCherry reporter expression for the Jurkat cells (Supplementary Fig. 9b) and by cytokine production (interferon (IFN)-γ and interleukin (IL)-2) and cytotoxicity for human T cells (Supplementary Fig. 9c,d). Once again, cytotoxicity of STOP-CAR-T cells (but not of 2G-CAR-T cells) was diminished by 10 μM Drug-2 (Supplementary Fig. 9d).

To evaluate whether our STOP-CAR approach has the potential to be generally applicable to other tumor antigens, we generated a CD19-targeted STOP-CAR (19-STOP-CAR) incorporating the well-characterized FMC63-derived scFv[33] onto the R-chain (Supplementary Fig. 10a), following the same design strategy as in Fig. 2a. Average co-transduction efficiencies of both R- and S-chains were 42% and 32% for primary human $CD4^+$ and $CD8^+$ T cells, respectively ($n = 6$–7 donors; Supplementary Fig. 10b). The expansion and effector and memory differentiation profile of bulk 19-STOP-CAR-T cells and 19-2G-CAR-T cells was similar to UTD-T cells (Supplementary Fig. 10c,e). Expression of the 19-STOP-CAR and effector function was stable (measured up to day 30) and upon co-culture with $CD19^+$ target cells, 19-STOP-CAR-T cells showed stable cytolytic capacity (even on day 30) and cytokine production largely similar to 2G-CAR-T cells (Supplementary Fig. 10d,f–h). Of note, pre-exposure to Drug-2 (10 μM) for just 12 h attenuated the cytotoxicity of 19-STOP-CAR-T cells (but not of 19-2G-CAR-T cells) against $CD19^+$ BV173 or Bjab target cells in co-cultures (where we did not add Drug-2 as target cells are also highly sensitive to Drug-2), demonstrating the functionality of the designed CDH in the context of an anti-CD19 CAR (Supplementary Fig. 10i,j).

Next, we tested the function of STOP-CAR-T cells in vivo using the anti-PSMA CARs as a model. We confirmed that daily injections of up to 5 mg kg^{-1} of Drug-2 (ref. [35]) were not acutely toxic to NSG mice, nor did they impair PC3-PIP tumor growth (Supplementary Fig. 11a,b). In a Winn assay, in which CAR-T cells were co-injected with tumor cells subcutaneously, both STOP- and 2G-CAR-T cells were able to fully control PC3-PIP tumor growth (Supplementary Fig. 11c). Furthermore, mice inoculated with 5×10^6 tumor cells and treated on day 5 by adoptive transfer of 2×10^6 2G-CAR-T cells or STOP-CAR-T cells exhibited excellent control of tumor growth in vivo, while the daily administration of Drug-2 disrupted STOP-CAR-T-cell activity, resulting in uncontrolled tumor growth (Fig. 3c and Supplementary Fig. 11d).

We further sought to evaluate whether a disruptor drug would dynamically control STOP-CAR-T cells, providing the basis for on-command T-cell therapy. In a drug pre-exposure assay in vitro (Fig. 3d), where CAR-T cells were exposed to Drug-2 transiently and then transferred in a drug-free environment, we saw that STOP-CAR-T cells fully regained both cytolytic activity and effector molecule secretion within 48 h (Fig. 3d,e and Supplementary Fig. 12). Moreover, in a dynamic in vivo assay we observed that withdrawal of Drug-2 after an initial period of administration enabled regain of STOP-CAR-T-cell activity and tumor control, resulting in a marked suppression of tumor growth relative to the period in which Drug-2 was applied. In contrast, delayed-onset exposure of mice to Drug-2 disrupted the ongoing activity of STOP-CAR-T cells in vivo, producing a marked tumor growth acceleration relative to the previous period when Drug-2 was not administered (Fig. 3f and Supplementary Fig. 11e). Thus, STOP-CAR-T cells control solid tumor growth with a similar efficacy as 2G-CAR-T cells in vivo and their activity can be tuned down specifically during the period of administration of a specific drug disruptor.

In summary, using a computational protein design approach, we developed a high-affinity CDH comprising only 11 interface amino acid substitutions relative to the initial human scaffold. We incorporated the CDH into a heterodimeric STOP-CAR that can specifically activate primary human T cells in the presence of target antigen. We observed that the default efficacy of STOP-CAR-T cells targeting PSMA or CD19 was at least equivalent to their respective conventional 2G-CAR-T cells. We observed at times superior cytolytic activity or IFN-γ response for the PSMA STOP-CAR than its 2G counterpart, but we believe this difference is idiosyncratic to this CAR and not generalizable to STOP-CAR designs.

Fig. 3 | STOP-CARs are functional in primary human T cells, both in vitro and in vivo and activity can be tuned in a dynamic drug-dependent manner. **a**, STOP-CAR-T cells (STOP) and 2G-CAR-T cells (2G) exhibit specific killing of antigen-expressing cells (PC3-PIP) but no cytotoxicity was observed against the isotype cell line (PC3). Values are the mean ± s.e.m. of $n = 5$ human donors. **b**, Killing of PC3-PIP tumor cells by UTD, 2G and STOP-CAR-T cells in the presence of 10 μM Drug-2. Values are the mean ± s.e.m. of $n = 5$ human donors. Cytotoxicity is reported as total area of dead cells, as measured by Cytotoxic Red reagent uptake (red area per μm^2). The effector to target cell ratio was 2:1. A two-way ANOVA with post hoc Tukey test was used for statistical analysis. Statistical significance: STOP versus STOP + Drug (20–30 h); $^{****}P \leq 0.0001$. **c**, Left: cartoon of the experimental design for in vivo experiments. NSG mice were subcutaneously (s.c.) inoculated with PC3-PIP tumor cells, and on day 5 received CAR-T cells or UTD-T cells, followed by daily s.c. injections of 10 μM Drug-2 or vehicle. Right: tumor growth is shown upon CAR-T cell transfer, with and without Drug-2. Values are the mean ± s.e.m. of $n = 5$ mice per group. A two-way ANOVA with post hoc Tukey test was used for statistical analysis. Statistical significance: considering all T-cell groups at day 16, $^{**}P = 0.0095$; STOP versus STOP + Drug at day 16, $^{****}P \leq 0.0001$. **d**, Left: schematic of the experimental approach for drug pre-exposure experiments; CAR-T cells were pre-incubated or not for 24 h with Drug-2, washed and rested for 48 h and then assessed for effector function. Right: STOP-CAR-T cell killing activity under different drug exposure conditions (Pre-Exp STOP, STOP-CAR-T cells pre-exposed to drug before functional assessment). Values are the mean ± s.e.m. of $n = 3$ human donors. Cytotoxicity is reported as total area of dead cells as measured by Cytotoxic Red reagent uptake (red area per μm^2). The effector to target cell ratio was 2:1. A two-way ANOVA with post hoc Tukey test was used for statistical analysis. Statistical significance: considering all T-cell groups, $^{*}P \leq 0.05$, $^{**}P \leq 0.01$, $^{****}P \leq 0.0001$. **e**, IFN-γ production of STOP-CAR-T cells. Values are the mean ± s.e.m. of $n = 3$ human donors. A one-way ANOVA was used for statistical analysis. Statistical significance: STOP versus Pre-Exp STOP $^{**}P \leq 0.040$; STOP or Pre-Exp STOP versus UTD $^{****}P \leq 0.0001$. **f**, Left: cartoon of the experimental design for in vivo dynamic responses. NOD SCIDγ (NSG) mice were s.c. inoculated with PC3-PIP tumor cells and on day 5 received CAR-T cells. One mouse group (dark green) received 10 μM Drug-2 from day 5–11, whereas another group (purple) received Drug-2 from day 11–17. A third group received no drug (pink). Drug was started or ended on day 11 due to a significant difference in tumor volume between STOP-CAR-T cells and STOP-CAR-T cells plus Drug-2. Right: STOP-CAR-T cells efficacy upon transient exposure to Drug-2. Values are mean ± s.e.m. of $n = 7$ mice per group. A one-way ANOVA with post hoc Tukey test was used for statistical analysis. Statistical significance at day 11: STOP versus STOP + Drug-2 day 5–11, $^{***}P = 0.0006$; STOP versus STOP + Drug-2 day 11–17, $P = 0.26$. Statistical significance at day 17: STOP versus STOP + Drug-2 day 5–11, $P = 0.2954$; STOP versus STOP + Drug-2 day 11–17, $^{**}P = 0.0054$.

The activity of the STOP-CAR-T cells was specifically impaired by a small-molecule drug disruptive to the CDH in a dynamic fashion upon drug administration, which was reversed upon drug removal. These results underscore that computational structure-based protein design holds great potential in the advancement of cellular therapies, both in terms of safety and function.

The STOP-CAR-T-cell data presented provide a proof-of-principle for a rationally designed safety mechanism with translational potential. In a clinical setting, we envision STOP-CARs as a tool to temporarily tune down T-cell activity in the event of an adverse patient response, while not eliminating the T cells, as is the case of a suicide switch. Controlled therapeutic modulation of CAR activity affords additional opportunities to accelerate the clinical development of first-in-human CARs with unknown safety profiles or to potentially prevent CAR-T-cell exhaustion from intense and prolonged exposure to antigen[36]. Important limitations still remain to fully understand the opportunity of STOP-CARs and to optimize their performance. The successful clinical application of STOP modules to prevent CAR toxicity arising from CRS or other on-target toxicities will depend on the speed and depth of CAR inactivation, whereas prevention of exhaustion could depend on our ability to fine tune CAR activity through intermittent drug administration. Thus, careful optimization of CAR and drug performance will be required for each envisioned application. Moreover, further optimization of the synthetic components may be necessary, such as eliminating neoepitopes that may emerge in the CAR proteins, to the extent that this is possible. This optimization process may be assisted by mature computational protein design tools, such as those

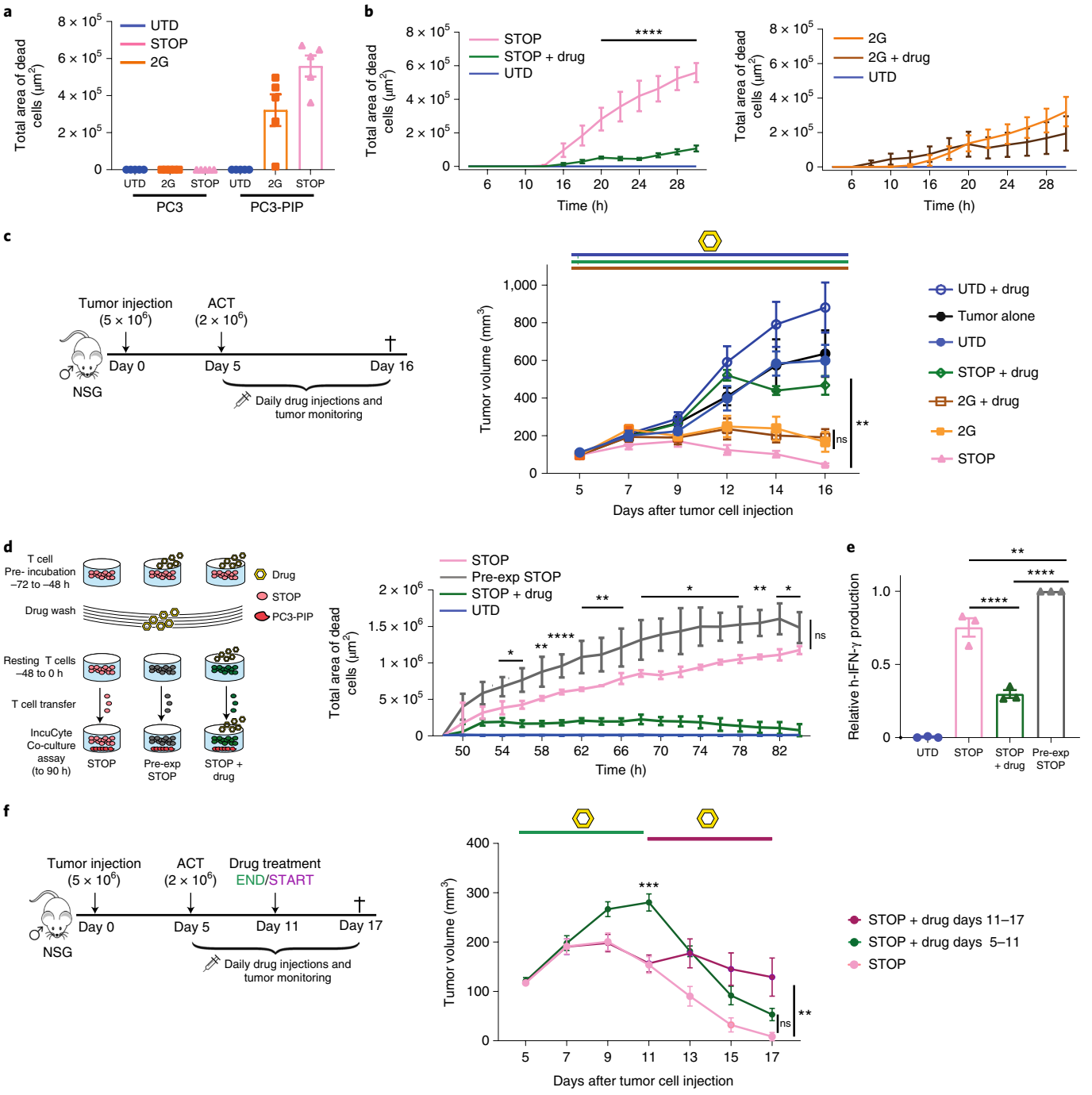

for T-cell epitope optimization[37,38]. In a broader context, our work demonstrates how rationally designed proteins can enable the use of clinically relevant drugs to control cellular processes, and can critically contribute to enlarge the toolbox available to synthetic biology and cell engineering[39].

Online content

Any methods, additional references, Nature Research reporting summaries, source data, extended data, supplementary information, acknowledgements, peer review information; details of author contributions and competing interests; and statements of data and code availability are available at https://doi.org/10.1038/s41587-019-0403-9.

Received: 13 November 2018; Accepted: 23 December 2019;
Published online: 3 February 2020

References

1. Kalos, M. et al. T cells with chimeric antigen receptors have potent antitumor effects and can establish memory in patients with advanced leukemia. *Sci. Transl. Med.* **3**, 95ra73 (2011).
2. Brentjens, R. J. et al. CD19-targeted T cells rapidly induce molecular remissions in adults with chemotherapy-refractory acute lymphoblastic leukemia. *Sci. Transl. Med.* **5**, 177ra138 (2013).
3. Maude, S. L. et al. Chimeric antigen receptor T cells for sustained remissions in leukemia. *N. Engl. J. Med.* **371**, 1507–1517 (2014).
4. Turtle, C. J. et al. CD19 CAR-T cells of defined $CD4^+$:$CD8^+$ composition in adult B cell ALL patients. *J. Clin. Invest.* **126**, 2123–2138 (2016).
5. Lim, W. A. & June, C. H. The principles of engineering immune cells to treat cancer. *Cell* **168**, 724–740 (2017).
6. Lanitis, E., Dangaj, D., Irving, M. & Coukos, G. Mechanisms regulating T cell infiltration and activity in solid tumors. *Ann. Oncol.* **28**, xii18–xii32 (2017).
7. Adachi, K. et al. IL-7 and CCL19 expression in CAR-T cells improves immune cell infiltration and CAR-T cell survival in the tumor. *Nat. Biotechnol.* **36**, 346–351 (2018).
8. Tang, L. et al. Enhancing T cell therapy through TCR-signaling-responsive nanoparticle drug delivery. *Nat. Biotechnol.* **36**, 707–716 (2018).
9. Morgan, R. A. et al. Case report of a serious adverse event following the administration of T cells transduced with a chimeric antigen receptor recognizing ERBB2. *Mol. Ther.* **18**, 843–851 (2010).
10. Gargett, T. & Brown, M. P. The inducible caspase-9 suicide gene system as a "safety switch" to limit on-target, off-tumor toxicities of chimeric antigen receptor T cells. *Front. Pharmacol.* **5**, 235 (2014).
11. Jones, B. S., Lamb, L. S., Goldman, F. & Di Stasi, A. Improving the safety of cell therapy products by suicide gene transfer. *Front. Pharmacol.* **5**, 254 (2014).
12. Fedorov, V. D., Themeli, M. & Sadelain, M. PD-1- and CTLA-4-based inhibitory chimeric antigen receptors (iCARs) divert off-target immunotherapy responses. *Sci. Transl. Med.* **5**, 215ra172 (2013).
13. Lanitis, E. et al. Chimeric antigen receptor T Cells with dissociated signaling domains exhibit focused antitumor activity with reduced potential for toxicity in vivo. *Cancer Immunol. Res.* **1**, 43–53 (2013).
14. Cho, J. H., Collins, J. J. & Wong, W. W. Universal chimeric antigen receptors for multiplexed and logical control of T cell responses. *Cell* **173**, 1426–1438 (2018).
15. Rodgers, D. T. et al. Switch-mediated activation and retargeting of CAR-T cells for B cell malignancies. *Proc. Natl Acad. Sci. USA* **113**, e459–e468 (2016).
16. Cartellieri, M. et al. Switching CAR-T cells on and off: a novel modular platform for retargeting of T cells to AML blasts. *Blood Cancer J.* **6**, e458 (2016).
17. Wu, C. Y., Roybal, K. T., Puchner, E. M., Onuffer, J. & Lim, W. A. Remote control of therapeutic T cells through a small molecule-gated chimeric receptor. *Science* **350**, aab4077 (2015).
18. Riddell, S. R. et al. T cell-mediated rejection of gene-modified HIV-specific cytotoxic T lymphocytes in HIV-infected patients. *Nat. Med.* **2**, 216–223 (1996).
19. Berger, C., Flowers, M. E., Warren, E. H. & Riddell, S. R. Analysis of transgene-specific immune responses that limit the in vivo persistence of adoptively transferred HSV-TK-modified donor T cells after allogeneic hematopoietic cell transplantation. *Blood* **107**, 2294–2302 (2006).
20. Jensen, M. C. et al. Antitransgene rejection responses contribute to attenuated persistence of adoptively transferred CD20/CD19-specific chimeric antigen receptor redirected T cells in humans. *Biol. Blood Marrow Transplant.* **16**, 1245–1256 (2010).
21. Boncompain, G. et al. Synchronization of secretory protein traffic in populations of cells. *Nat. Methods.* **9**, 493–498 (2012).
22. Rollins, C. T. et al. A ligand-reversible dimerization system for controlling protein–protein interactions. *Proc. Natl Acad. Sci. USA* **97**, 7096–7101 (2000).
23. Bouillet, P. & Strasser, A. BH3-only proteins: evolutionarily conserved proapoptotic Bcl-2 family members essential for initiating programmed cell death. *J. Cell Sci.* **115**, 1567–1574 (2002).
24. Leverson, J. D. et al. Exploiting selective BCL-2 family inhibitors to dissect cell survival dependencies and define improved strategies for cancer therapy. *Sci. Transl. Med.* **7**, 279ra240 (2015).
25. Hinds, M. G. et al. BIM, Bad and Bmf: intrinsically unstructured BH3-only proteins that undergo a localized conformational change upon binding to prosurvival Bcl-2 targets. *Cell Death Differ.* **14**, 128–136 (2007).
26. Procko, E. et al. A computationally designed inhibitor of an Epstein–Barr viral Bcl-2 protein induces apoptosis in infected cells. *Cell* **157**, 1644–1656 (2014).
27. Gemperli, A. C., Rutledge, S. E., Maranda, A. & Schepartz, A. Paralog-selective ligands for Bcl-2 proteins. *J. Am. Chem. Soc.* **127**, 1596–1597 (2005).
28. Chin, J. W. & Schepartz, A. Design and evolution of a miniature Bcl-2 binding protein. *Angew. Chem. Int. Ed. Engl.* **40**, 3806–3809 (2001).
29. Silva, D. A., Correia, B. E. & Procko, E. Motif-driven design of protein–protein interfaces. *Methods Mol. Biol.* **1414**, 285–304 (2016).
30. Ku, B., Liang, C., Jung, J. U. & Oh, B. H. Evidence that inhibition of BAX activation by Bcl-2 involves its tight and preferential interaction with the BH3 domain of BAX. *Cell Res.* **21**, 627–641 (2011).
31. Lanier, L. L. DAP10- and DAP12-associated receptors in innate immunity. *Immunol. Rev.* **227**, 150–160 (2009).
32. Ghosh, A., Wang, X., Klein, E. & Heston, W. D. Novel role of prostate-specific membrane antigen in suppressing prostate cancer invasiveness. *Cancer Res.* **65**, 727–731 (2005).
33. Kochenderfer, J. N. et al. Construction and preclinical evaluation of an anti-CD19 chimeric antigen receptor. *J. Immunother.* **32**, 689–702 (2009).
34. Santoro, S. P. et al. T cells bearing a chimeric antigen receptor against prostate-specific membrane antigen mediate vascular disruption and result in tumor regression. *Cancer Immunol. Res.* **3**, 68–84 (2015).
35. Tao, Z. F. et al. Discovery of a potent and selective Bcl-XL inhibitor with in vivo activity. *ACS Med. Chem. Lett.* **5**, 1088–1093 (2014).
36. Feucht, J. et al. Calibration of CAR activation potential directs alternative T cell fates and therapeutic potency. *Nat. Med.* **25**, 82–88 (2019).
37. Griswold, K. E. & Bailey-Kellogg, C. Design and engineering of deimmunized biotherapeutics. *Curr. Opin. Struct. Biol.* **39**, 79–88 (2016).
38. Zhao, H. et al. Depletion of T cell epitopes in lysostaphin mitigates anti-drug antibody response and enhances antibacterial efficacy in vivo. *Chem. Biol.* **22**, 629–639 (2015).
39. Gainza-Cirauqui, P. & Correia, B. E. Computational protein design — the next generation tool to expand synthetic biology applications. *Curr. Opin. Biotech.* **52**, 145–152 (2018).

Methods

Computational design. The design of the Bcl-XL binders was performed using a side-chain grafting approach[29] . Several crystal structures have revealed the drug-binding pocket targeted by multiple drugs that inhibit the Bcl-XL–BIM-BH3 binding interaction[24]. Additionally, peptides derived from BIM-BH3 have also been crystallized in complex with Bcl-XL, occupying the same binding pocket[40]. To design new binders that could be competed by available small-molecule drugs, we used the Bcl-XL–BIM-BH3 complex to search for proteins that could fulfill two criteria: (1) backbone conformation that mimicked the BIM-BH3 peptide, which was fully helical; and (2) a three-dimensional topology that was compatible with the Bcl-XL structure to allow a productive binding interaction. After candidate protein scaffolds were found, the hotspot side chains were transplanted to the scaffolds and additional design was performed in the interfacial positions of the putative scaffolds. Specifically, for the designs presented here, we selected 12 residues that form the binding motif of BIM-BH3 to Bcl-XL (residues 90 to 101). Residues 90, 91, 94, 97, 98 and 101 (BH3 numbering) were selected as hotspot residues and their identities were maintained, whereas the remaining residues in the binding motif and interface were allowed to mutate. The scaffold search was performed in a subset of the PDB that fulfilled all the following criteria: (1) monomeric proteins with one chain in the biological assembly; (2) length between 80 and 160 residues; (3) presence of helical motifs; and (4) structures determined by X-ray crystallography. These filters resulted in a database of 11,012 proteins to be searched as potential scaffolds.

The design protocol was encoded using the RosettaScripts interface[41] and consisted of the following steps: (1) MotifGraft searched for structural matches of the helical segment of BIM-BH3 in the scaffold database that presented ≤1.0 Å backbone r.m.s.d.; and (2) if a backbone match was found, steric compatibility with the scaffold and Bcl-XL was assessed and scaffolds whose backbone clashed with the seed or with the target Bcl-XL were discarded. Scaffolds that fulfilled the matching criteria were carried to the design stage and hotspot residues and side-chain conformations that were transplanted to the scaffold and nonhotspot residues within 6 Å of Bcl-XL were allowed to mutate to any amino acid with a positive score according to the BLOSUM62 matrix[42]. This sequence constraint was utilized to minimize changes from the original scaffold. The design procedure consisted of two rounds of sequence design[43] intercalated by two rounds of side-chain continuous minimization[44], including small changes to the protein dihedral angles within their energy wells, which allow them to escape steric clashes[45].

The final list of designs was ranked by the Rosetta predicted change in Gibbs free energy after complex formation (ddG) and designs with a ddG superior to −10 Rosetta energy units (REU) were not considered. This resulted in a list of 85 designed scaffolds. Our visual inspection of the resulting designs led us to apply extra filters to remove proteins that were not globular and showed extended conformations with designed binding motifs with very poor packing to the rest of the protein scaffold. As a first filter to select globular proteins we used a metric proposed by Miller et al.[46], which found that the solvent-accessible surface area A_s of globular proteins correlates well with the mass M of the protein, under the power law:

$$A_s = 6.3M^{0.73}$$

We used this power law to judge whether designed scaffolds were globular proteins or not. To filter for globularity, scaffolds whose ratio $A_s/6.3M^{0.73}$ was below a cutoff of 0.8 were removed from consideration.

As a second filter we also quantified the packing interactions of the binding motif with the remaining scaffold. To do so, we measured two structural features: (1) number of van der Waals (vdW) contacts with binding segment and the scaffold, using the probe program[47]; and (2) buried surface area of the binding segment in the context of the scaffold. Scaffolds whose number of vdW contact dots between seed and scaffold was less than 900 or where the 'buried surface area' of the seed upon grafting was less than 4,000, were discarded. These thresholds were determined empirically based on the metrics for well-packed seeds. Out of the 85 scaffolds selected by ddG, only 11 passed the packing and globularity filters.

After manual inspection and comparison to the original BIM-BH3 domains, two human and one rat protein (with a human homolog) scaffolds were selected from this list: rat Syntaxin 6 (PDB ID: 1LVF, chain A) (LD1), Human Focal Adhesion Targeting Domain (PDB ID: 3GM2, chain A) (LD2) and the human apolipoprotein E4 mutant (PDB ID: 1LE4, chain A) (LD3). Three residues in LD1 and four residues in LD2 were manually reverted to their identity in the native scaffold as they were found to not interact with the target. In the case of LD3 an Ala residue in the interface was mutated to Gln in a second design run by Rosetta (Supplementary Fig. 1).

Protein expression and purification. The gene sequences of Bcl-XL and all the designed proteins were flanked with an N-terminal 6XHis-tag and synthesized by GenScript. Genes were cloned into a pET-11b expression vector by using Gibson assembly (New England Biolabs, E2611S). The sequence-confirmed plasmid was transformed into *Escherichia coli* BL21 (DE3) (Thermo Fisher) and a single clone was used to inoculate 700 ml of Terrific Broth (101629, Merck Millipore) containing ampicillin (100 μg ml^{-1}). The culture was grown at 37 °C until OD_{600} reached around 1.0 and protein expression was induced with 1 mM IPTG (Fisher Scientific) at 20 °C. After overnight induction, cells were collected by centrifugation at 4,000 r.p.m. and the bacterial pellet was resuspended in 40 ml of lysis buffer (50 mM Tris, 500 mM NaCl and 5% glycerol at pH 7.5) containing 100 μg ml^{-1} PMSF (ROTH, 6376.2) and 1 mg ml^{-1} lysozyme (10837059001, Sigma-Aldrich). The cells were disrupted by sonication and lysates were cleared by centrifuging at 20,000*g* for 20 min. Cleared lysate was loaded onto an AKTA purifier (GE Healthcare) for Ni-NTA affinity purification. The column was washed with five column values of equilibration buffer (50 mM Tris, 500 mM NaCl and 20 mM imidazole) and the protein was eluted in equilibration buffer supplemented with 300 mM imidazole. The eluent was further purified by gel filtration with a Superdex 75 10/300 GL column (GE Healthcare) in phosphate buffer (pH 7.4). The purified proteins were concentrated, aliquoted and stored at −80 °C.

Compounds. Drug-2 (A115546399.5%, Chemietek CT-A115) and Drug-1 (A1331852, 99.5%, Chemietek CT-A133) were directly used without further purification. A1155463 and A1331852 were each dissolved in DMSO as 10 mM stocks. Stocks were aliquoted and stored at −20 °C until use.

Circular dichroism. Folding of the designed scaffolds and Bcl-XL was measured using circular dichroism spectroscopy. Protein samples were dissolved in a phosphate saline buffer at a protein concentration of around 0.2 mg ml^{-1} (20 μM). The sample was loaded into a 0.1-cm path-length quartz cuvette (Hellma). The far-UV CD spectrum between 190 nm and 250 nm was recorded by a J-815 spectrometer (Jasco) with a slit band-width of 2.0 nm, with a scanning speed at 20 nm min^{-1}. Response time was set to 0.125 s and spectra were averaged from two individual scans.

Size-exclusion chromatography coupled with multi-angle light scattering. LD3 and Bcl-XL were characterized by SEC-MALS to determine solution state and to study dimerization and drug-induced monomerization properties. LD3 and Bcl-XL were injected at 50–100 μM in PBS or reducing elution buffer (5 mM Tris, 50 mM NaCl and 5 mM 2-mercaptoethanol), respectively, on a SuperdexTM 75 300/10 GL column (GE Healthcare) using an high-performance liquid chromatography system (Ultimate 3000, Thermo Scientific) with a flow rate of 0.5 ml min^{-1}. The UV spectrum at 280 nm was collected along with static light scatter signal by a MALS device (miniDAWN TREOS, Wyatt). For determining the drug-induced monomerization, 50 μM Bcl-XL was mixed with equimolar LD3. Either DMSO alone or Drug-2 (A1155463, ChemieTek) at 10 mM in DMSO was added to a final concentration of 100 μM (twofold excess) and samples were directly analyzed by SEC-MALS in PBS to detect complex formation and forced dissociation. The light scatter signal of the sample was collected from three different angles and the result was analyzed by the Wyatt evaluation software (ASTRA v.6).

Surface plasmon resonance. SPR data were collected on a Biacore 8 K device (GE Healthcare). Bcl-XL was immobilized on a CM5 biosensor chip (GE Healthcare) at a 5 μg ml^{-1} concentration in different acetate solutions (GE Healthcare) at pH 4.5 to reach a final surface ligand density of around 300 response units (RUs). Serial dilutions of LD3 and other designs in HBS-EP + buffer (10 mM HEPES, 150 mM NaCl, 3 mM EDTA and 0.005% Surfactant P20; GE Life Science) were injected as an analyte. After each injection cycle, surface regeneration was performed using 10 mM NaOH (pH 11.95). Affinity (K_d) and kinetic parameters (K_{on} and K_{off}) were obtained using a 1:1 Langmuir binding model, unless otherwise noted, with Biacore 8 K evaluation software. For the drug competition assay, 4 μM of analyte proteins were pre-incubated with serially diluted concentrations of Drug-1 and Drug-2, starting from an initial concentration of 0.01 nM for both. Multiple-cycle injections of the protein–drug complex with different stoichiometry were performed to measure the decrease of maximal RUs. Apparent IC_{50} was obtained using the inhibition versus response fitting models in PRISM software.

Purification of Bcl-2 and LD3 for crystallization. The Bcl-2 protein used in this study is a chimeric protein containing human Bcl-2 (residues 1–50 and 92–207) and human Bcl-XL (residues 35–50) that replaces a long loop in Bcl-2 (residues 51–91)[48]. The *LD3* gene was cloned as described above. Both proteins were produced with an N-terminal 6x(His) tag in the *E. coli* BL21 (DE3) RIPL strain (Novagen) at 18 °C overnight. Cell lysate in a buffer solution containing 20 mM Tris-HCl (pH 7.5) and 100 mM NaCl was loaded onto Co-NTA resin (Thermo Scientific) and the proteins were eluted with the buffer solution containing 150 mM imidazole. While the 6x(His) tag on LD3 was uncleavable, that of Bcl-2 was cleaved with the TEV protease. The two proteins were further purified by using a HiTrap Q anion exchange column (GE Healthcare).

Preparation, crystallization and structure determination of the Bcl-2–LD3 complex. Purified Bcl-2 (0.9 mg ml^{-1}) was mixed with LD3 (4.9 mg ml^{-1}) in a 1:1 molar ratio and the complex between the two proteins was isolated by gel filtration using a HiLoad 26/60 Superdex 75 (GE Healthcare). The crystals of the resulting complex were obtained by the hanging-drop vapor diffusion method at 22 °C by mixing and equilibrating 2 μl of each of the complex (24.3 mg ml^{-1}) and a precipitant solution containing 17% PEG2000, 0.1 M sodium succinate (pH 5.5)

and 0.32 M ammonium sulfate. Before data collection, the crystals were immersed briefly in a cryoprotectant solution, which was the reservoir solution containing additional 12.5% glycerol. A diffraction dataset at 2.5 Å was collected at 100 K with X-ray wavelength of 1.0000 Å on the beam line 11C at the Pohang Accelerator Laboratory, Korea. The structure was determined by the molecular replacement method with the Phaser-MR[49] in the PHENIX suite[50] using the structures of BCL-2 (ref. [48]) and apolipoprotein E (PDB ID: 1LE4 (ref. [51])) as search models. Subsequently, model building and refinement were carried out using the programs COOT[52] and CNS[53]. The final model does not include residues 1–8, 32–48 (including the entire Bcl-XL substitution region) and 165–166 of BCL-2, and residues 1–9 and 151–156 of LD3, whose electron densities were not observed or were very weak. Crystallographic data statistics are summarized in Supplementary Table 1.

The coordinates of the Bcl-2–LD3 structure will be deposited in the PDB and released immediately upon publication.

Cell lines. The prostate carcinoma cell lines, 22Rv1 ($PSMA^{lo}$), PC3-PIP ($PMSA^{hi}$) and PC3 ($PSMA^{-}$), 293T human embryonic kidney (HEK-293T), Jurkat cell lines, BV173 and Bjab were cultured in RPMI-1640 supplemented with 10% heat-inactivated fetal bovine serum (FBS), 2 mmol l^{-1} L-glutamine, 100 µg ml^{-1} penicillin and 100 U ml^{-1} streptomycin, at 37 °C in a 5% CO_2 atmosphere (Invitrogen, Life technologies). HEK-293T, 22Rv1, Jurkat and Bjab cell lines were purchased from the American Type Culture Collection. PC3-PIP and PC3 cell lines were provided by A. Rosato (University of Padua, Padova)[32]. MS1 and $PSMA^{+}$-MS1 cells were obtained from the University of Pennsylvania. BV173 was provided by C. Arber (Ludwig Cancer Center, University of Lausanne). The HEK-293T cell line was used for lentiviral packaging and preparation. Jurkat reporter cells were developed by lentiviral transduction to stably express 6xNFAT-mCherry such that upon activation they turn red.

STOP-CAR construction. The two STOP-CAR chains, R-chain and S-chain, were synthesized as gene strings (GeneArt, Thermo Fischer Scientific) and cloned into a third-generation self-inactivating lentiviral expression vector, pELNS, with expression driven by the elongation factor-1α (EF-1α) promoter. The anti-PSMA scFv derived from monoclonal antibody J591 and the anti-CD19 CAR scFv derived from monoclonal antibody FMC63 were used as the tumor-targeting moiety[33,54]. The R-chain comprises a CD8α leader sequence, anti-PSMA scFv (or anti-CD19 scFv), CD8α hinge, CD28 TMD, CD28 ED and a serine-glycine (SG) linker, LD3. The S-chain consists of a CD8α leader sequence, c-Myc, DAP10 ectodomain, CD8α hinge, CD28 TMD, CD28 ED, SG linker, Bcl-XL, SG linker and CD3ζ ED.

Recombinant lentivirus production. High-titer replication-defective lentivirus was produced and concentrated by ultracentrifugation for primary T-cell transduction. Briefly, 24 h before transfection, HEK-293 cells were seeded at 10×10^6 in 30 ml of medium in a T-150 tissue culture flask. All plasmid DNA was purified using the Endo-free Maxiprep kit (Invitrogen, Life Technologies). HEK-293T cells were transfected with 7 µg pVSV-G (VSV glycoprotein expression plasmid), 18 µg of R874 (Rev and Gag/Pol expression plasmid) and 15 µg of pELNS transgene plasmid, using a mix of Turbofect (Thermo Fisher Scientific AG) and Optimem medium (Invitrogen, Life Technologies, 180 µl of Turbofect for 3 ml of Optimem). The viral supernatant was collected 48 h after transfection. Viral particles were concentrated by ultracentrifugation for 2 h at 24,000*g* and resuspended in 400 µl of complete RPMI-1640 medium, followed by immediate snap freezing on dry ice.

Jurkat cell transduction. Jurkat cells were suspended at 1×10^6 cells per ml and seeded into 48-well plates at 500 µl per well. For each transduction, 50 µl of virus supernatant was used. After incubation for 24 h at 37 °C the cell medium was refreshed, and the cells were incubated for an additional 72 h at 37 °C before use.

Primary human T-cell transduction. Primary human T cells were isolated from the peripheral blood mononuclear cells of healthy donors (HDs; prepared as buffycoats or apheresis filters). All blood samples were collected with informed consent of the HDs, and genetically engineered with ethics approval from the Canton of Vaud to the laboratory of G. Coukos. Total peripheral blood mononuclear cells were obtained via Lymphoprep (Axonlab) separation solution, using a standard protocol of centrifugation. $CD4^{+}$ and $CD8^{+}$ T cells were isolated using a magnetic bead-based negative selection kit following the manufacturer's recommendations (easySEP, Stem Cell technology). Purified $CD4^{+}$ and $CD8^{+}$ T cells were cultured at a 1:1 ratio in RPMI-1640 with Glutamax, supplemented with 10% heat-inactivated FBS, 100 U ml^{-1} penicillin and 100 µg ml^{-1} streptomycin sulfate and stimulated with anti-CD3 and anti-CD28 monoclonal antibody (mAb)-coated-beads (Invitrogen, Life Technologies) in a ratio of 1:2 T cells to beads. T cells were transduced with lentivirus particles at 18–22 h after activation. Human recombinant IL-2 (h-IL-2; Glaxo) was replenished every other day for a concentration of 50 IU ml^{-1} until 5 d after stimulation (day +5). At day +5, magnetic beads were removed, and h-IL-7 and h-IL-15 (Miltenyi Biotec GmbH) were added to the cultures at 10 ng ml^{-1} replacing h-IL-2. A cell density of $0.5–1 \times 10^6$ cells ml^{-1} was maintained for expansion. Rested engineered T cells were adjusted for equivalent transgene expression before all functional assays.

Nuclei red PC3-PIP transduction. To generate a PC3-PIP stably nonperturbing nuclear restricted red fluorescent label we used 0.2 ml of IncuCyte NucLight Red Lentivirus Reagent (EF-1α, Puro; Sartorius). Briefly, PC3-PIP was seeded in a 48-well plate and allowed to adhere overnight. The day after, when cell confluence was almost 30%, NucLight Red Lentivirus Reagent was added to the medium together with polybrene, following the IncuCyte protocol for infection. Medium was replaced after 24 h. Puromicyn was added every other day at 1 µg ml^{-1} for 1 week to allow red clone selection. Nuclei Red PC3-PIP were analyzed by flow cytometry before cytotoxicity assays.

Cytokine release assays. Cytokine release assays were performed by co-culture of 5×10^4 T cells with 5×10^4 target cells per well in 96-well round-bottom plates, in duplicate, in a final volume of 200 µl of RPMI medium. After 24 h, the co-culture supernatants were collected and tested for the presence of IFN-γ and IL-2 by commercial enzyme-linked immunosorbent assay kits according to the manufacturer's protocol (BioLegend). Values were normalized to the maximum value (set to 1) for each donor to eliminate variability due to other factors, such as age and sex among HDs. The reported values represent the mean of cytokine production by STOP-CAR-engineered T cells derived from HDs ± s.e.m.

Alternatively, cytokines in the co-culture supernatants were quantified using the Cytokine Bead Array kit (BD Bioscience) and flow cytometric analysis, following the manufacturer's recommendation. Data were analyzed with FlowJo software, v.10.

Cytotoxicity assays. Cytotoxicity assays were performed using the IncuCyte Instrument (Essen Bioscience). Briefly, 1.25×10^4 target cells were seeded in flat-bottom 96-well plates (Costar, Vitaris). Four hours later, rested T cells (no cytokine addition for 48 h) were washed and seeded at 2.5×10^4 per well, at a 2:1 effector to target ratio in complete medium. No exogenous cytokines were added during the co-culture period of the assay. Cytotox Red reagent (Essen Bioscience) was added at a final concentration of 125 nM in a total volume of 200 µl. Alternatively, a nuclei red PC3-PIP stable cell line expressing a nuclear restricted red fluorescent label was used for the assays. Internal experimental negative controls were included in all assays, including co-incubation of UTD-T cells and tumor cells, as well as tumor cells alone, in the presence of Cytotox Red reagent to monitor spontaneous cell death over time. As a positive control, tumor cells alone were treated with 1% triton solution to evaluate maximal killing in the assay. Images of total red area per well were collected every 2 h of the co-culture. The total red area per well was obtained by using the same analysis protocol on the IncuCyte ZOOM software provided by Essen Bioscience. All data were normalized by subtracting the background fluorescence observed at time 0 (before any cell killing by CAR-T cells) from all further time points. Data are expressed as the mean of different HDs ± s.e.m.

Short-term cytotoxicity was performed by quantitative flow cytometry acquisition. Briefly, 1.25×10^4 target cells were seeded in U-bottom 96-well plates (Costar, Vitaris). Rested T cells (untreated or preconditioned with 10 µM Drug) were seeded at 1.25×10^4 per well at 1:1 effector to target ratio and then incubated at 37 °C for 4 h. Cells were collected, washed and stained with antibodies targeting CD3 and CD19, as well as a LIVE/DEAD marker (Thermo Fisher Scientific). Flow cytometry acquisition was kept at constant speed and normalized for the same time of sample running (30 s per tube). Residual live $CD3^{-}CD19^{+}$ target cells were quantified and used as the final readout.

Flow cytometric analysis. To evaluate cell-surface expression of the heterodimeric STOP-CAR, transduced cells were stained with fluorescenated anti-human F(ab') mAb to detect the R-chain and fluorescenated anti-human c-Myc mAb to detect the S-chain. Aqua live Dye BV510 and near-infrared fluorescent reactive dye (APC-Cy-7) were used to assess viability (Invitrogen, Life Technologies). The following mAbs (BD, Bioscience) were used for phenotypic memory analysis: BV711 mouse-anti-human CD3; BV605 mouse-anti-human CD4; APC-Cy-7-labeled anti-human CD8; PE-Texas red-labeled mouse-anti-human CD45RA; and BV421 mouse-anti-human CCR7. For evaluating STOP-CAR chain expression, gating was performed to isolate live single cells. To determine memory phenotype, the $CD3^{+}$ population was first gated, followed by the $CD4^{+}$ and $CD8^{+}$ subsets, which were then evaluated for CD45RA and CCR7 expression to determine the percentage of naive (T_N), central memory (T_{CM}), effector memory (T_{EM}) and terminally differentiated (T_{EMRA}) T cells. Tumor cell-surface expression of PSMA and CD19 were quantified by fluorescently labeled anti-human-PSMA and anti-human-CD19 mAbs. Isotype control staining was employed. Acquisition and analysis was performed using a BD FACS LSRII and FACS DIVA software (BD Biosciences), respectively. AMNIS imaging of transduced Jurkat cells stained with FITC-labeled anti-human F(ab') and APC-labeled anti-human c-Myc, was used to evaluate colocalization of the R- and S-chains of the STOP-CAR. IDEAs software was used to analyze the data and perform the colocalization analysis after gating on live (DAPI negative), single cells that are double-positive for FITC and APC.

Mice and in vivo experiments. NSG mice were bred and housed in a specific and opportunistic pathogen-free animal facility in the Oncology Department of the University of Lausanne. All experiments were conducted according to the Swiss Federal Veterinary Office guidelines and were approved by the Cantonal Veterinary Office. All cages housed five animals in an enriched environment providing free access to food and water. During experimentation, all animals were monitored at least every other day for signs of distress. Mice were killed at the endpoint by carbon dioxide overdose.

In vivo drug toxicity testing. NSG males, aged 8–12 weeks, were shaved in the right flank and treated daily with 50-µl s.c. injections of A1155463 (Drug-2) dissolved at 1.25 mg kg^{-1} or 2.5 mg kg^{-1} in a solution of saline and 2% dimethyl sulfoxide (DMSO) or vehicle (2% DMSO in saline). The animals were monitored daily and weighed to assess any signs of drug toxicity. To determine the potential effect of Drug-2 on in vivo tumor control, five mice per group were s.c. injected with 5×10^6 PC3-PIP tumor cells. At day 4, when the tumors were palpable, daily peritumoral injections of 2.5 mg kg^{-1} or 5 mg kg^{-1} of Drug-2 or vehicle were administered. The animals were monitored daily and the tumors were calipered every other day. Tumor volumes were calculated using the formula $V=1/2(\text{length}\times\text{width}^2)$, where length is the greatest longitudinal diameter and width is the greatest transverse diameter determined via caliper measurement.

Winn assay. For a preliminary evaluation of tumor control by STOP-CAR-T cells in comparison to 2G-CAR-T cells, a Winn assay was performed in which 8–12 week-old NSG males were s.c. injected with 3×10^6 PC3-PIP tumor cells, mixed with either saline or 3×10^6 UTD, STOP-CAR or 2G-CAR-T cells. The tumor volume was evaluated via caliper measurement every other day.

Subcutaneous therapeutic prostate tumor model. To evaluate the therapeutic potential of STOP-CAR-T cells, 8–12-week-old NSG males were s.c. injected with 5×10^6 PC3-PIP tumor cells. Once palpable (day 5), the mice were grouped for similar mean tumor volume and standard deviation and then treated by peritumoral injection of 2×10^6 T cells (UTD, 2G-CAR or STOP-CAR-T cells). At 2 h after T-cell transfer, a peritumoral injection of Drug-2 at 5 mg kg^{-1} was performed. Injections of the drug were then provided daily until the endpoint. In the dynamic control experiments, Drug-2 was administered from day 5–11 or from day 11 until the endpoint. Tumor volume was assessed every other day by caliper measurement.

Statistical analysis. An unpaired Student's *t*-test and Mann–Whitney *U*-test were used to evaluate differences in absolute numbers of T cells (expansion over 10 d), T cells in each memory category, transferred number of T cells analyzed ex vivo and cytokine secretion. All data are represented as mean ± s.e.m. A two-way ANOVA with post hoc Tukey test was used to evaluate significant differences in specific cytolysis in vitro and tumor growth in vivo. A one-way ANOVA was used to evaluate significant differences in short-term cytotoxicity experiments for CD19-targeting CAR-T cells and dynamic in vivo tumor control with anti-PSMA CAR-T cells. GraphPad Prism 7.0 (GraphPad Software) was used for statistical calculations. $P\leq0.05$ was considered significant. Levels of significance are: $^*P\leq0.05$, $^{**}P\leq0.01$, $^{***}P\leq0.001$ and $^{****}P\leq0.0001$. Additional statistical information is in the Supplementary Table.

DNA sequences of CAR constructs. The DNA sequences of the CAR constructs used in this paper are presented in Supplementary Note 1.

Reporting Summary. Further information on research design is available in the Nature Research Reporting Summary linked to this article.

Data availability

The data supporting the findings of this study are available within the article and its Supplementary Information. Coordinates of the determined structure have been deposited in the PDB with accession code 6IWB. Other data are available from the corresponding authors upon reasonable request.

Code availability

All code used to perform the design simulation can be found at https://github.com/LPDI-EPFL/STOP-CAR.

References

40. Lee, E. F. et al. High-resolution structural characterization of a helical αβ-peptide foldamer bound to the anti-apoptotic protein Bcl-XL. *Angew. Chem. Int. Ed. Engl.* **48**, 4318–4322 (2009).
41. Fleishman, S. J. et al. RosettaScripts: a scripting language interface to the Rosetta macromolecular modeling suite. *PLoS ONE* **6**, e20161 (2011).
42. Henikoff, S. & Henikoff, J. G. Amino acid substitution matrices from protein blocks. *Proc. Natl Acad. Sci. USA* **89**, 10915–10919 (1992).
43. Kuhlman, B. & Baker, D. Native protein sequences are close to optimal for their structures. *Proc. Natl Acad. Sci. USA* **97**, 10383–10388 (2000).
44. Wang, C., Schueler-Furman, O. & Baker, D. Improved side-chain modeling for protein–protein docking. *Protein Sci.* **14**, 1328–1339 (2005).
45. Gainza, P., Roberts, K. E. & Donald, B. R. Protein design using continuous rotamers. *PLoS Comput. Biol.* **8**, e1002335 (2012).
46. Miller, S., Janin, J., Lesk, A. M. & Chothia, C. Interior and surface of monomeric proteins. *J. Mol. Biol.* **196**, 641–656 (1987).
47. Word, J. M. et al. Visualizing and quantifying molecular goodness-of-fit: small-probe contact dots with explicit hydrogen atoms. *J. Mol. Biol.* **285**, 1711–1733 (1999).
48. Petros, A. M. et al. Solution structure of the antiapoptotic protein Bcl-2. *Proc. Natl Acad. Sci. USA* **98**, 3012–3017 (2001).
49. McCoy, A. J. et al. Phaser crystallographic software. *J. Appl. Crystallogr.* **40**, 658–674 (2007).
50. Adams, P. D. et al. PHENIX: a comprehensive Python-based system for macromolecular structure solution. *Acta Crystallogr. D* **66**, 213–221 (2010).
51. Dong, L. M. et al. Human apolipoprotein E. Role of arginine 61 in mediating the lipoprotein preferences of the E3 and E4 isoforms. *J. Biol. Chem.* **269**, 22358–22365 (1994).
52. Emsley, P. & Cowtan, K. Coot: model-building tools for molecular graphics. *Acta Crystallogr. D* **60**, 2126–2132 (2004).
53. Brunger, A. T. et al. Crystallography and NMR system: a new software suite for macromolecular structure determination. *Acta Crystallogr. D* **54**, 905–921 (1998).
54. Gong, M. C., Chang, S. S., Sadelain, M., Bander, N. H. & Heston, W. D. Prostate-specific membrane antigen (PSMA)-specific monoclonal antibodies in the treatment of prostate and other cancers. *Cancer Metastasis Rev.* **18**, 483–490 (1999).

Acknowledgements

This work was generously supported by the Biltema and ISREC Foundations, an Advanced European Research Council Grant to G.C. (no. 1400206AdG-322875), a Starting European Research Council Grant to B.E.C. (no. 716058), the National Center of Competence for Molecular Systems Engineering, the Ludwig Institute for Cancer Research, EPFL-Fellows grants funded by an H2020 Marie Sklodowska-Curie action to P.G. and J.B., as well as a Whitaker International fellowship to E.G.G. B.-H.O. was supported by the National Research Foundation of Korea (NRF-2018R1A2B3004764). We thank members of the Flow Cytometry Platform and the Animal Care Facility of the University of Lausanne for their excellent support. Computational calculations were performed using the facilities of the Scientific IT and Application Support Center of EPFL. We also acknowledge the EPFL Protein Production and Structure Core Facility for providing access to biophysical instrumentation. Finally, we thank S. Maerkl, M. Lutolf and E. Procko for critical reading of the manuscript and E. Oricchio for valuable discussions.

Author contributions

G.G.-A., E.G.-G., E. C. and S.S. designed and performed experiments and interpreted results. P.G. performed computational design and interpreted results. S.V., A.J.C.O. and P.R. assisted with the experimental work. J.B. assisted the computational design. S.K., M.K. and B.-H.O. performed X-ray crystallography and structure determination. G.G.-A., E.G.-G. and P.G. wrote the manuscript. M.I., G.C. and B.E.C. designed and supervised the study, interpreted results and wrote the manuscript.

Competing interests

EPFL, UNIL and the Ludwig Institute for Cancer Research have filed for patent protection on the technology described herein. G.G.-A., P.G., M.I., G.C. and B.E.C. are named as co-inventors on this patent (United States Patent and Trademark Office Provisional Application: 62/657,534).

Additional information

Supplementary information is available for this paper at https://doi.org/10.1038/s41587-019-0403-9.

Correspondence and requests for materials should be addressed to M.I., G.C. or B.E.C.

Reprints and permissions information is available at www.nature.com/reprints.

nature research

Corresponding author(s): Bruno Correia, George Coukos, Melita Irving

Reporting Summary

Nature Research wishes to improve the reproducibility of the work that we publish. This form provides structure for consistency and transparency in reporting. For further information on Nature Research policies, see Authors & Referees and the Editorial Policy Checklist.

Statistical parameters

When statistical analyses are reported, confirm that the following items are present in the relevant location (e.g. figure legend, table legend, main text, or Methods section).

n/a	Confirmed	
☐	☒	The exact sample size (*n*) for each experimental group/condition, given as a discrete number and unit of measurement
☐	☒	An indication of whether measurements were taken from distinct samples or whether the same sample was measured repeatedly
☐	☒	The statistical test(s) used AND whether they are one- or two-sided *Only common tests should be described solely by name; describe more complex techniques in the Methods section.*
☒	☐	A description of all covariates tested
☐	☒	A description of any assumptions or corrections, such as tests of normality and adjustment for multiple comparisons
☐	☒	A full description of the statistics including central tendency (e.g. means) or other basic estimates (e.g. regression coefficient) AND variation (e.g. standard deviation) or associated estimates of uncertainty (e.g. confidence intervals)
☐	☒	For null hypothesis testing, the test statistic (e.g. *F*, *t*, *r*) with confidence intervals, effect sizes, degrees of freedom and *P* value noted *Give P values as exact values whenever suitable.*
☒	☐	For Bayesian analysis, information on the choice of priors and Markov chain Monte Carlo settings
☒	☐	For hierarchical and complex designs, identification of the appropriate level for tests and full reporting of outcomes
☒	☐	Estimates of effect sizes (e.g. Cohen's *d*, Pearson's *r*), indicating how they were calculated
☐	☒	Clearly defined error bars *State explicitly what error bars represent (e.g. SD, SE, CI)*

Our web collection on statistics for biologists may be useful.

Software and code

Policy information about availability of computer code

Data collection	IncuCyte Instrument, BD LSR II FACS, BD LSR SORP FACS, AMNIS INSPIRE for ISX mk II, Biacore 8K
Data analysis	IncuCyte Zoom 2016A Data analysis (Essen Bioscience), FACS DIVA Software, Microsoft Excel for Mac 2017, GraphPad Prism v7, FlowJo X, AMINIS IDEAS. All the design calculations were performed with Rosetta. Molecular visualization and image rendering were done with Pymol. The structure was determined with Phaser in the PHENIX software suite.

For manuscripts utilizing custom algorithms or software that are central to the research but not yet described in published literature, software must be made available to editors/reviewers upon request. We strongly encourage code deposition in a community repository (e.g. GitHub). See the Nature Research guidelines for submitting code & software for further information.

Data

Policy information about availability of data

All manuscripts must include a data availability statement. This statement should provide the following information, where applicable:

- Accession codes, unique identifiers, or web links for publicly available datasets
- A list of figures that have associated raw data
- A description of any restrictions on data availability

The authors declare that data supporting the findings of this study are available within the article and its Supplementary Information. Coordinates of the structure determined have been deposited in the PDB with the accession code XXXX. Other data are available from the corresponding authors upon reasonable request.

Field-specific reporting

Please select the best fit for your research. If you are not sure, read the appropriate sections before making your selection.

☒ Life sciences ☐ Behavioural & social sciences ☐ Ecological, evolutionary & environmental sciences

For a reference copy of the document with all sections, see nature.com/authors/policies/ReportingSummary-flat.pdf

Life sciences study design

All studies must disclose on these points even when the disclosure is negative.

Sample size	For the in vitro studies number of healthy donors and/or technical replicates were chosen according to the complexity of the assay and for the expected biological variability. For the in vivo studies maximum of 2 millions CAR T cells/mouse were needed. We achieved a sample size of 5 animal per treatment group which proved to be sufficient to reproducibly observe statistically significant differences.
Data exclusions	For the in vivo studies, upon calipering outlier mice with extreme burdens (either too high or too low compared to the average) were excluded from the experiment before CAR T cell transfer. No mice were excluded afterwards at any point.
Replication	All attempts at replication were successful. Anti-tumor activity could vary between T cell donor, both in vitro and in vivo.
Randomization	Tumor burden was evaluated by calipering the same day of CAR T cell transfer. Outlier mice with extreme burdens (either too high or too low compared to the average) were excluded from the experiment before CAR T cell transfer. No mice were excluded afterwards at any point. Following tumor burden measure, mice were assigned into treatment groups such that each group had the same overall average tumor volume. Buffy coats and apheresis filters were obtained from anonymous donors.
Blinding	To minimize stress to the mice, treatment administration and tumor volume measurements were made at the same time (during same anaesthesia). An independent investigator verified caliper measurements in a blinded fashion. Analysis of data (plotting of pre-recorded tumor volumes at end of study) was performed in a non-blinded manner.

Reporting for specific materials, systems and methods

Materials & experimental systems

n/a	Involved in the study
☒	☐ Unique biological materials
☐	☒ Antibodies
☐	☒ Eukaryotic cell lines
☒	☐ Palaeontology
☐	☒ Animals and other organisms
☐	☒ Human research participants

Methods

n/a	Involved in the study
☒	☐ ChIP-seq
☐	☒ Flow cytometry
☒	☐ MRI-based neuroimaging

Antibodies

Antibodies used	Antibodies were titrated for optimal staining. Aqua live Dye BV510 (L34966, Invitrogen, Lot no 1930868) and near-IR fluorescent reactive dye (APC Cy-7) (L34976, Invitrogen, lot no 2013787) were used to assess viability. The following fluorophore conjugated antibodies were used for phenotypic memory analysis: BV711 mouse-anti-human CD3 (clone UCHT1, cat 563725, lot no 7026609, BD, Bioscience); BV605 mouse-anti-human CD4 (clone OKT4, cat 317438, lot no B236686,Biolegend); APC-Cy7-labeled

anti-human CD8 (clone SK1, cat A94683, lot no 23, Beckman Coulter); PE-Texas red-labeled mouse-anti-human CD45RA (clone HI100, cat B49193, lot no 4, Beckman Coulter); BV421 mouse-anti-human CCR7 (clone G043H7, cat 353208, lot no B254502, Biolegend). AMNIS imaging of transduced Jurkat cells stained was performed with FITC-labeled anti-human F(ab)' (cat 115-095-072, lot no 132090, Jackson Immuno Research) APC-labeled anti-human cMyc (cat MCA2200A647, lot no 0414, Bio-Rad). AlexaFluo 647-conjugated anti-mouse F(ab)' (cat 115-606-072, lot no 130184, Jackson Immuno Research) and APC-labeled anti-human cMyc (clone 9E10, cat MCA2200A647, lot no 0414, Bio-Rad) or FITC-labeled anti-human cMyc (clone 9E10, cat MAB4518, lot no 531513, Abnova) were used to evaluate the expression of the R- and S-chains of the STOP-CAR on primary T cells. PE-labeled anti-human PSMA (clone LNI-17, cat 342504, lot no B211500, Biolegend) and PE Isotype mouse-anti-IgG1, k chain (clone MOPC-21, cat 400114, lot no B202580, Biolegend) were used to evaluated PSMA expression on cell line. PE-labeled anti-human CD19 (clone HIB19, cat 302208, lot no B171136, Biolegend) was used to evaluate CD19 expression on cell lines and in the context of short term cytotoxicity assay by FACS, together with BV421-labeled anti-human CD3 (clone OKT3, cat 317343, lot no B264956, Biolegend).

Validation

Antibody concentration validation was empirically determined in the lab.

Eukaryotic cell lines

Policy information about cell lines

Cell line source(s)

293T, Jurkat, Bjab and 22Rv1 from ATCC. PC3 and PC3-PIP from Dr. Rosato, University of Padova. MS1 and MSI-PSMA+ from Dr. Coukos from University of Pennsylvania. Jurkat 6x-NFAT mCherry were engineered in the lab. BV173 from Dr.Arber, LICR, University of Lausanne.

Authentication

COA provided with cell line by ATCC. Properties pertinent to experiment (e.g. PSMA expression) were confirmed by flow cytometry.

Mycoplasma contamination

All cell lines were routinely tested for mycoplasma contamination and found negative.

Commonly misidentified lines
(See ICLAC register)

No cell lines from the ICLAC register were used.

Animals and other organisms

Policy information about studies involving animals; ARRIVE guidelines recommended for reporting animal research

Laboratory animals

NSG male mice, 8-12 weeks old, were bred and housed in a SOPF animal facility.

Wild animals

N/A

Field-collected samples

N/A

Human research participants

Policy information about studies involving human research participants

Population characteristics

Buffy coats and apheresis filters from anonymous healthy donors were collected with informed consent of the donors, and genetically engineered with Ethics Approval from the Canton of Vaud.

Recruitment

N/A

Flow Cytometry

Plots

Confirm that:

☒ The axis labels state the marker and fluorochrome used (e.g. CD4-FITC).

☒ The axis scales are clearly visible. Include numbers along axes only for bottom left plot of group (a 'group' is an analysis of identical markers).

☒ All plots are contour plots with outliers or pseudocolor plots.

☒ A numerical value for number of cells or percentage (with statistics) is provided.

Methodology

Sample preparation

Primary human T cells were isolated from the peripheral blood mononuclear cells (PBMCs) of healthy donors (HDs; prepared as buffycoats or apheresis filters). All blood samples were collected with informed consent of the HDs, and genetically-engineered with Ethics Approval from the Canton of Vaud to the laboratory of Dr. Coukos. Total PBMCs were obtained via Lymphoprep (Axonlab) separation solution, using a standard protocol of centrifugation. CD4+ and CD8+ T cells were isolated using a magnetic bead-based negative selection kit following the manufacturer's recommendations (easySEP, Stem Cell technology). Purified CD4+

and CD8+ T cells were cultured at a 1:1 ratio in RPMI-1640 with Glutamax, supplemented with 10% heat-inactivated FBS, 100 U/mL penicillin, 100 µg/mL streptomycin sulfate, and stimulated with anti-CD3 and anti-CD28 monoclonal antibody (mAb)-coated-beads (Lifetechnologies) in a ratio of 1:2, T cells: beads. For staining preparation, cells were washed once and resuspended in FACS buffer containing LIVE/DEAD dye and the antibody cocktail. Cells were incubated at 4 degrees for 30 minutes and washed twice before acquisition. Cells were not fixed prior to acquisition. For short time cytotoxicity assay, CD19+ target cells (Bjab and BV173) were seeded at 12500 cells/well in 100 µL of complete RPMI media. Untransduced and transduced T cells (previously incubated or not with 10 µM A1155463 for 12 hours, and then washed to remove Drug from the culture media) were counted and seeded 12500 cells/well in 100 µL complete RPMI media and then added on tumor cells. After 5 hours of coculture cells were washed once and resuspended in FACS buffer containing LIVE/DEAD dye and the antibody cocktail (anti-CD3 and anti-CD19). Cells were incubated at 4 degrees for 30 minutes and washed twice before quantitative acquisition. Cells were not fixed prior to acquisition.

Instrument

LSR II, BD

Software

Collection: FACS DIVA
Analysis: FlowJo X

Cell population abundance

T cell purification from PBMCs by magnetic beads was validated by flow for CD4+/CD8+ cells. T cell purity was >99%.

Gating strategy

Starting cell population was gated on a linear SSC-A/FSC-A plot. Single cells were discriminated on a linear FSC-H/FSC-A plot. Live cells were determined by exclusion from positive Live/Dead stained cells. Positive/Negative populations were determined with negative controls.

☒ Tick this box to confirm that a figure exemplifying the gating strategy is provided in the Supplementary Information.